IN-34
19772
P 43

Comparison of SMAC, PISO, and Iterative Time-Advancing Schemes for Unsteady Flows

Sang-Wook Kim
University of Texas at Arlington
Arlington, Texas

and

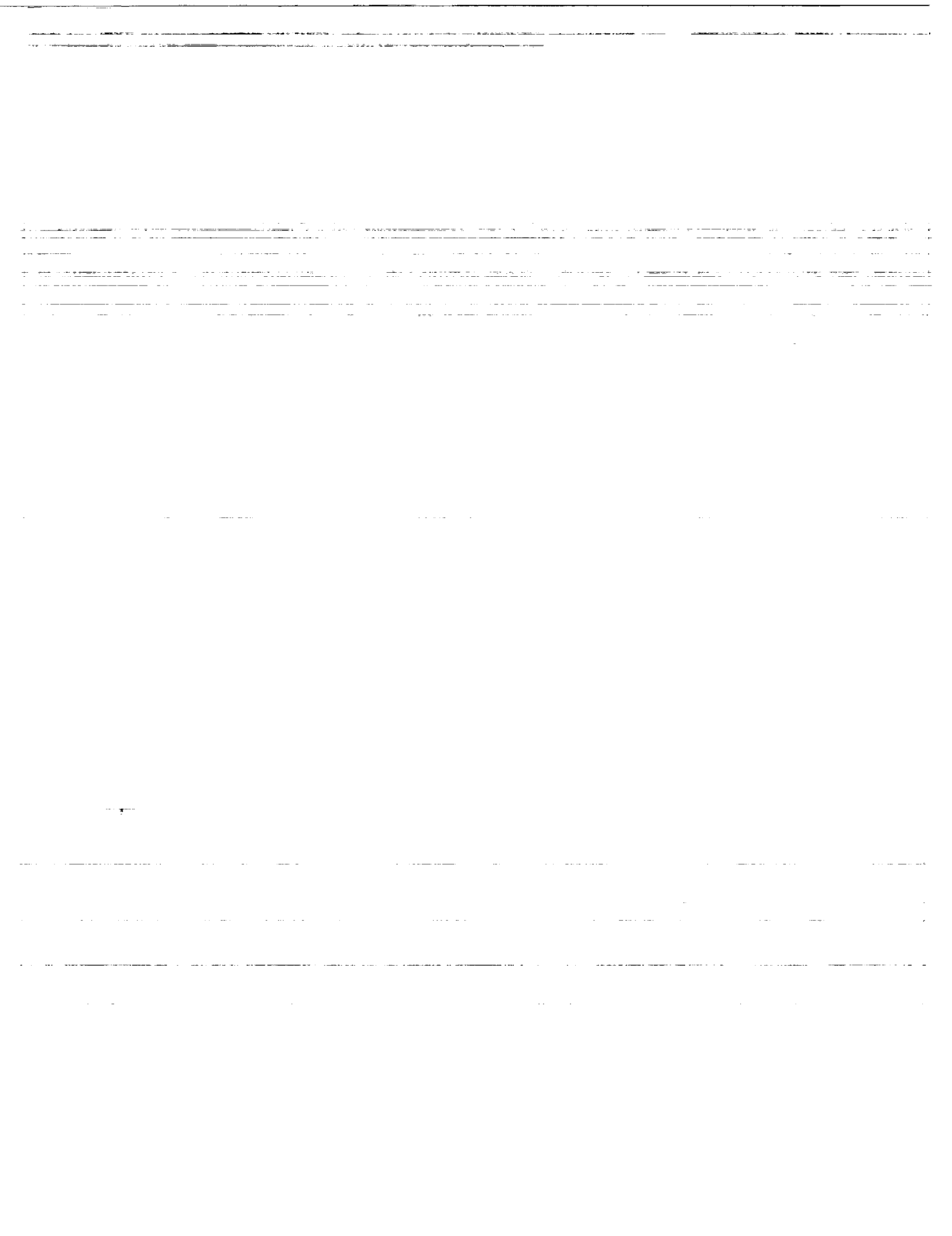Thomas J. Benson
Lewis Research Center
Cleveland, Ohio

June 1991

NASA

COMPARISON OF SMAC, PISO, AND ITERATIVE TIME-ADVANCING

SCHEMES FOR UNSTEADY FLOWS

Sang-Wook Kim*
University of Texas at Arlington
Department of Aerospace Engineering
Arlington, Texas 76010

and

Thomas J. Benson
National Aeronautics and Space Administration
Lewis Research Center
Cleveland, Ohio 44135

SUMMARY

Calculations of unsteady flows using a simplified marker and cell (SMAC), a pressure-implicit splitting of operators (PISO), and an iterative time-advancing scheme (ITA) are presented. A partial differential equation for incremental pressure is used in each time-advancing scheme. Example flows considered are a polar cavity flow starting from rest and self-sustained oscillatory flows over a circular and a square cylinder. For a large time-step size, the SMAC and ITA are more strongly convergent and yield more accurate results than PISO. The SMAC is the most efficient computationally. For a small time-step size, the three time-advancing schemes yield equally accurate Strouhal numbers. The capability of each time-advancing scheme to accurately resolve unsteady flows is attributed to the use of a new pressure correction algorithm that can strongly enforce the conservation of mass. The numerical results show that the low frequency of the vortex shedding is caused by the growth time of each vortex shed into the wake region.

---

*Resident Research Associate at NASA Lewis Research Center.

NOMENCLATURE

A_i	coefficient for u_i velocity of discrete momentum equation
b	side of square cylinder
C_i	coefficient for temporal discretization (i=1,2,3)
f	frequency, f=1/T
L	reference length
p	pressure
r	radius of circular cylinder
r_y	normal distance measured from bottom wall of polar cavity
T	period of vortex shedding
t	time
U_o	reference velocity
u_i	velocity component, u_i={u,v}
x_j	cartesian coordinates
Δ	increment
θ	angle (unit in degree)
μ	molecular viscosity
ρ	density
$\sum$	summation
τ	non-dimensional time, $\tau = tU_o/L$

superscript

n	time-level

subscript

nb	neighboring grid points

INTRODUCTION

For incompressible flows, the conservation of mass acts as a constraint condition that the velocity field needs to satisfy; while in compressible flows, the conservation of mass is given as a partial differential equation for the temporal variation of density. Due to this distinct difference, recent developments of numerical methods to solve compressible flows are mostly concentrated on unsteady Navier-Stokes equations while those for incompressible flows are mostly concentrated on steady Navier-Stokes equations. Thus the numerical methods to solve unsteady incompressible flows have been reported only sporadically even though one of the earliest numerical methods to solve an unsteady, incompressible flow appeared as early as 1965 [1].

A careful examination of various unsteady incompressible flow solution techniques can provide a valuable guideline for a further extension of these numerical methods to solve more complex unsteady flow problems. The accuracy, convergence nature, and computational effort of SMAC [2], PISO [3,4] and ITA are examined by solving a polar cavity flow [5] starting from rest and self-sustained oscillatory flows over a circular cylinder [2] and a square cylinder [6].

The ITA is a direct extension of steady flow solution techniques to solve unsteady flows. In the method, a steady flow solution technique is used iteratively to obtain a converged solution for each time-level. Therefore, the ITA can be computationally heavy.

The marker and cell (MAC) scheme was originally developed to solve an unsteady free-surface flow. The method was simplified to solve an unsteady laminar flow over a circular cylinder by Braza et al. [2] and a few other flow cases cited in the reference. The name "marker and cell"

has been retained in Ref. [2] and in the present study even though the numerical method itself has nothing to do with the "marker and cell" for the unsteady flows considered in these studies. Two slightly different schemes, varying in the complexity of the pressure equation, have been presented in Ref. [2]. The more complex case requires almost the same computational effort as that of PISO while the accuracy remains the same as that of the simpler case, and hence only the simpler case is considered herein. The simpler case is recast in a discrete form so that the context may be consistent with the other time-advancing schemes.

The PISO [3] was proposed to avoid the heavy computational effort of ITA. Calculations of a laminar flow through a suddenly expanding pipe and a compressible flow entering a suddenly expanding closed pipe can be found in [4]. In the present study, the PISO [3,4] is modified to be memory efficient, which results in a slightly increased computational effort than the original PISO. For clarity, the modified PISO is described in detail in this paper.

In the pressure correction algorithm used in this paper, the incremental pressure is obtained by solving a partial differential equation for incremental pressure, which yields a strongly diagonally dominant system of equations for the incremental pressure. It has been shown in a number of numerical calculations of various two- and three-dimensional flows that the present method yields strongly and highly convergent results even when highly graded and skewed meshes are used to discretize the flow domain [7-10]. For example, the pressure correction algorithm yields a grid independent solution for a 3-D curved duct flow with a very small number of grid points and it can reduce the mass imbalance at least a few orders of magnitude smaller than those

4

obtainable using various other pressure correction algorithms [9].

NUMERICAL METHODS

The incompressible laminar flow equations are given as;

$$\frac{\partial u_j}{\partial x_j} = 0. \tag{1}$$

$$\frac{\partial(\rho u_i)}{\partial t} + \frac{\partial}{\partial x_j}(\rho u_i u_j) - \frac{\partial}{\partial x_j}\left\{\mu(\frac{\partial u_i}{\partial x_j} + \frac{\partial u_j}{\partial x_i})\right\} = -\frac{\partial p}{\partial x_i} \tag{2}$$

where $\rho u_i u_i$ and $\rho u_i u_j$ $(i \neq j)$ represent the nonlinearity in each component of the momentum equation and the nonlinear coupling between the u_i- and u_j-velocity, respectively. Repeated indices imply summation over the index unless otherwise stated.

The unsteady flow solution techniques are implemented on a pressure-staggered mesh and the incremental pressure is obtained by solving a partial differential equation for incremental pressure. Only a few necessary details of the present pressure correction algorithm are summarized in "Iterative Time-Advancing Scheme" sub-section even though the same pressure correction algorithm is used for each of the unsteady flow solution techniques. Details on the pressure correction algorithm can be found in Refs. [7-9].

The transient term in the momentum equation is treated implicitly. The temporal variation of ρu_i can be discretized as

$$\frac{\partial(\rho u_i)}{\partial t} = \rho C_1 u_i^n - \rho C_2 u_i^{n-1} + \rho C_3 u_i^{n-2} \tag{3}$$

5

where $(C_1, C_2, C_3) = (1/\Delta t, 1/\Delta t, 0)$ and $(3/2\Delta t, 4/2\Delta t, 1/2\Delta t)$ for the first and the second order difference approximations, respectively. Since a few different time-advancing techniques are discussed below, the consistency of a few notations related to each time-advancing scheme is confined to each time-advancing scheme and each of such notations is explained only when it appears for the first time in each sub-section.

Iterative Time-Advancing Scheme (ITA)

The initial guesses for the new time-level velocity (u_i^*) and pressure (p^*) are set equal to those of the previous time-level. The discrete momentum equation based on the guessed flow variables can be written as

$$(\rho C_1 + A_i^*)u_i^{**} = \sum_{nb} \{A_k^* u_k^{**}\} + S_i^* - \frac{\partial p^*}{\partial x_i} + \rho C_2 u_i^{n-1} - \rho C_3 u_i^{n-2},$$

$$\text{no sum on i,} \qquad (4)$$

where u_i^{**} is a predicted velocity, A_i^* is the coefficient of the u_i^{**}-velocity, S_i^* is a source term originating from a skewed mesh, and the coefficients A_i^* and S_i^* are evaluated using the initial guess. The predicted velocities are obtained by solving eq. (4). The predicted velocities are not necessarily divergence free, and hence the velocities are corrected to satisfy the conservation of mass. Let u_i^{***} and p^{**} are the corrected velocity and pressure that satisfy the conservation of mass. Then

$$u_i^{***} = u_i^{**} + u'_i, \qquad (5)$$

$$p^{**} = p^* + p' \qquad (6)$$

6

where p' is the incremental pressure. The discrete momentum equations which satisfy the conservation of mass can be written as

$$(\rho C_1 + A_i^*)u_i^{***} - \sum_{nb} (A_k^* u_k^{***}) + S_i^* - \frac{\partial p^{**}}{\partial x_i} + \rho C_2 u_i^{n-1} - \rho C_3 u_i^{n-2},$$

no sum on i, (7)

Subtracting eq. (4) from eq. (7) yields;

$$u_i' = - \frac{1}{(\rho C_1 + A_i^*)} \frac{\partial p'}{\partial x_i},$$ no sum on i, (8)

where the pressure gradient is left in continuous form deliberately. It is discussed later that the velocity-pressure decoupling that occurs when various pressure correction algorithms are used for a pressure-staggered mesh is caused by using a discretized pressure gradient in eq. (8) in deriving the discrete pressure correction equation. In deriving eq. (8), the summation over the neighboring grid points are disregarded. Retaining the residual originating from the neighboring grid points cause the numerical results to depend on the under-relaxation parameter [9]. Applying the conservation of mass to eq. (5) yields

$$\frac{\partial u'_j}{\partial x_j} = - \frac{\partial u_j^{**}}{\partial x_j} \qquad (9)$$

Substituting eq. (8) into eq. (9) yields a partial differential equation for the incremental pressure given as;

$$\frac{\partial}{\partial x_j} \left\{ \frac{1}{(\rho C_1 + A_j^*)} \frac{\partial p'}{\partial x_j} \right\} = \frac{\partial u_j^{**}}{\partial x_j} \qquad (10)$$

7

where the last term in eq. (10) represents the mass imbalance. The incremental pressure is obtained by solving eq. (10) and the velocities and pressure are corrected using eqs. (5) and (6), respectively. The above procedure needs to be iterated using u_i^{***} and p^{**} as new initial guesses until the differences between the old and the new corrected velocities and pressures, respectively, become negligibly small; and the converged solutions represent the flow field of the current time-level.

A single iteration of the ITA can not account for the nonlinearity in the momentum equation. However, the flow equations are solved iteratively until the convergence criteria are met at each time-level, the nonlinearity in each component of the momentum equation and the nonlinear coupling of u-and v-velocity are fully accounted for in the method.

In each of the time-advancing schemes discussed in this paper, the incremental pressure is obtained by solving a partial differential equation for the incremental pressure. As all the central-differenced finite volume equations for self-adjoint second order elliptic partial differential equations are strongly diagonally dominant, the present discrete pressure correction equation is strongly diagonally dominant even for a highly skewed mesh. On the other hand, consider deriving a discrete pressure correction equation from eq. (8) using a discretized pressure gradient in eq. (8). Substituting eq. (8) into eq. (9) and integrating it over a pressure control volume yields a system of equations for incremental pressure which is not diagonally dominant. In such a case, the mass imbalance for a particular pressure grid point produces large pressure corrections for the adjacent pressure grid

points, and the velocity-pressure decoupling occurs. In case a discrete

pressure gradient is used in eq. (8) to derive a system of discrete

pressure correction equations, only a fully-staggered mesh or the

momentum interpolation schemes [11-12] can yield a diagonally dominant

system of equations for the incremental pressure. However, the

fully-staggered mesh is not an optimal grid layout for complex

geometries; and the momentum interpolation scheme can not account for the

grid skewness and it also yields a numerical result that depends on the

under-relaxation parameter unless a specialized interpolation scheme is

adopted [9,12]. However, the present pressure correction scheme does not

yield a numerical result that depends on the under-relaxation parameter,

since eq. (10) clearly states that the incremental pressure is driven

only by the mass imbalance.

Simplified Marker and Cell Scheme (SMAC)

The SMAC and PISO are non-iterative time-advancing schemes and

hence, an initial guess is not necessary for these schemes. The discrete

momentum equations based on the flow variables of the previous time-level

can be written as

$$(\rho C_1 + A_i^{n-1})u_i^* = \sum_{nb}(A_k^{n-1}\ u_k^*) + S_i^{n-1} - \frac{\partial p^{n-1}}{\partial x_i} + \rho C_2 u_i^{n-1} - \rho C_3 u_i^{n-2},$$

$$\text{no sum on i,} \quad (11)$$

where u_i^* is the predicted velocity, A_i^{n-1} is the coefficient of the

u_i^*-velocity, S_i^{n-1} is a source term originating from a skewed mesh, and

the coefficients A_i^{n-1} and S_i^{n-1} are evaluated using the flow variables

of the previous time-level. The predicted velocities are obtained by

9

solving eq. (11). The predicted velocity field may not satisfy the conservation of mass, thus the predicted velocities need to be corrected to satisfy the conservation of mass. Let $u_i{}^n$ be the velocity that satisfy the conservation of mass. Then

$$u_i^n - u_i^* = -\frac{\partial \phi}{\partial x_i},$$ (12)

where ϕ is an auxiliary potential field. Taking divergence of eq. (12) yields

$$\frac{\partial}{\partial x_j}\left\{\frac{\partial \phi}{\partial x_j}\right\} - \frac{\partial u_j^*}{\partial x_j} = 0$$ (13)

which can be solved in the same way as that for eq. (10). The divergence free velocity field for the current time-level is obtained using eq. (12). In the SMAC, the search for the flow field of the current time-level is concluded by obtaining a consistent pressure (p^*) that satisfies the momentum equation. The discrete momentum equation for the current time-level can be written as

$$(\rho C_1 + A_i^{n-1})u_i^n = \sum_{nb}\{A_k^{n-1}u_k^n\} + S_i^{n-1} - \frac{\partial p^n}{\partial x_i} + \rho C_2 u_i^{n-1} - \rho C_3 u_i^{n-2}$$

no sum on i (14)

Subtracting eq. (11) from eq. (14) yields;

$$\rho C_1(u_i^n - u_i^*) = -\frac{\partial}{\partial x_i}(p^n - p^{n-1}),$$ (15)

where A_i^{n-1} has been disregarded since $A_i^{n-1} \ll \rho C_1$ for a very small

time-step size. Substituting eq. (12) into (15) yields

$$- \frac{\partial}{\partial x_i} (\rho C_1 \phi) = - \frac{\partial}{\partial x_i} (p^n - p^{n-1})$$

or

$$p^n = p^{n-1} + \rho C_1 \phi \qquad (16)$$

where the spatial variation of C_1 has been neglected.

In eq. (14), the coefficients of the u_i^n-velocity and the source term originating from a skewed mesh have not been updated. Thus SMAC can not account for the nonlinearity in each component of the momentum equation. It also can not account for the nonlinear coupling of u- and v-velocity unless the discrete u- and v-momentum equations are solved simultaneously as a single system of equations.

The velocity field obtained using the SMAC satisfy the conservation of mass strongly at each time-level. However, due to the use of an over-simplified pressure equation, eq. (16), the velocity and pressure fields may not satisfy the conservation of momentum rigorously. In fact, the over-simplified pressure equation can overshoot the pressure and it may yield a non-physical solution when the second order temporal discretization is used. On the other hand, the use of the first order temporal discretization always yields as accurate numerical results as those obtainable using the ITA or PISO incorporating the second order temporal discretization. This unusual behavior of the SMAC indicates that the second order temporal discretization is not quite compatible with the over-simplified momentum equation.

A more elaborate SMAC presented in Ref. [2] has also been tested in the course of the present study, however, any significant improvement in

accuracy was not observed. The same observation has also been expressed in Ref. [2]. On the other hand, the computational effort of the alternative scheme becomes comparable to that of the PISO.

Pressure-Implicit Separation of Operators (PISO)

The discrete momentum equation based on the flow variables of the previous time-level can be written as

$$(\rho C_1 + A_i^{n-1})u_i^* = H_i^* - \frac{\partial p^{n-1}}{\partial x_i} + \rho C_2 u_i^{n-1} - \rho C_3 u_i^{n-2}, \quad \text{no sum on i,} \quad (17)$$

where

$$H_i^* = \sum (A_k^{n-1} u_k^*) + S_i^{n-1}$$

and the notations used in eq. (17) are the same as those for eq. (11). The predicted velocity is obtained by solving eq. (17). The predicted velocity field is not necessarily divergence free, and hence the velocity field needs to be corrected to satisfy the conservation of mass. Let u_i^{**} and p^* are the first corrected velocity and pressure that satisfy the conservation of mass, respectively. Then

$$u_i^{**} = u_i^* + u_i', \quad (18)$$

$$p^* = p^{n-1} + p' \quad (19)$$

where u'_i and p' are the first incremental velocity and pressure, respectively. The discrete momentum equations which satisfy the conservation of mass can be written as

$$(\rho C_1 + A_i^{n-1})u_i^{**} = H_i^* - \frac{\partial p^*}{\partial x_i} + \rho C_2 u_i^{n-1} - \rho C_3 u_i^{n-2}, \quad \text{no sum on i,} \quad (20)$$

12

Subtracting eq. (17) from eq. (20) yields;

$$u_i' = -\frac{1}{(\rho C_1 + A_i^{n-1})}\frac{\partial p'}{\partial x_i}, \quad \text{no sum on } i, \tag{21}$$

where the summation over the neighboring grid points and the source term originating from a skewed mesh have been disregarded in deriving eq. (21). Applying the conservation of mass to eq. (18) yields

$$\frac{\partial u'_j}{\partial x_j} = -\frac{\partial u_j^*}{\partial x_j} \tag{22}$$

Substituting eq. (21) into eq. (22) yields a partial differential equation for the incremental pressure given as;

$$\frac{\partial}{\partial x_j}\left\{\frac{1}{(\rho C_1 + A_j^{n-1})}\frac{\partial p'}{\partial x_j}\right\} = \frac{\partial u_j^*}{\partial x_j} \tag{23}$$

where the last term in eq. (23) represents the mass imbalance. The first incremental pressure is obtained by solving eq. (23), the first corrected pressure is obtained from eq. (19), and the first corrected velocity is obtained using eqs. (18) and (21). The first corrected velocity may satisfy the conservation of mass, but it does not satisfy the momentum equation according to Ref. [3,4]. Let the velocity and pressure that satisfy the momentum equation be u_i^{***} and p^{**}, where u_i^{***} and p^{**} are the second corrected velocity and pressure, respectively. The discrete momentum equation based on the second corrected velocity and pressure can be written as

13

$$(\rho C_1 + A_i^{**})u_i^{***} = H_i^{**} - \frac{\partial p^{**}}{\partial x_i} + \rho C_2 u_i^{n-1} - \rho C_3 u_i^{n-2} , \quad \text{no sum on } i, \quad (24)$$

where

$$H_i^{**} - \sum_{nb} (A_k^{**} u_k^{**}) + S_i^{**} ,$$

A_i^{**} and S_i^{**} are evaluated using the first corrected velocity, and the momentum equation has been written in an explicit form to correct the velocity and pressure without solving a system of equations. Subtracting eq. (20) from eq. (24) yields;

$$(\rho C_1 + A_i^{**})u_i^{''} - H_i^{**} - H_i^{*} - \frac{\partial p^{''}}{\partial x_i} , \quad \text{no sum on } i, \quad (25)$$

where A_i^{n-1} can be set equal to A_i^{**} without incurring large error since $A_j^{**} \ll \rho C_1$ and

$$u_i^{''} - u_i^{***} - u_i^{**} \quad (26)$$

$$p^{''} - p^{**} - p^{*} \quad (27)$$

are the second incremental velocity and pressure, respectively. Inserting eq. (25) into eq. (26) and taking divergence of eq. (26) yields;

$$\frac{\partial}{\partial x_j} \left\{ \frac{1}{(\rho C_1 + A_j^{**})} \frac{\partial p^{''}}{\partial x_j} \right\} - \frac{\partial}{\partial x_j} \left\{ \frac{1}{(\rho C_1 + A_j^{**})} (H_j^{**} - H_j^{*}) \right\} , \quad (28)$$

The second incremental pressure is obtained by solving eq. (28), the second corrected pressure is obtained from eq. (27), and the second corrected velocity is obtained from eqs. (25) and (26).

The present PISO algorithm is slightly different from that of Issa [3] in the load vector term of eq. (28). In the original PISO algorithm,

the coefficients of the discrete momentum equation need to be stored to evaluate the load vector in eq. (29). In the present PISO algorithm, only the resultant given as $H^{**}-H^*$ needs to be stored to solve the second pressure correction equation. The present method is more memory efficient than the original PISO, while it requires more computational efforts. This modification has been motivated by the experience, obtained from numerical calculations of three-dimensional flows [9-10], that the required memory to solve complex three-dimensional flows may easily exceeds the current computer capacity. The modified PISO can better account for the nonlinearity in each component of the momentum equation since the updated residuals are used in solving the second pressure correction equation.

In the first corrector step of the PISO, the velocity and pressure are corrected to satisfy the conservation of mass. In the second corrector step, the velocity and pressure are corrected to satisfy the momentum equation. Therefore, the driving force of the second pressure corrector step is obtained from the momentum imbalance even though the pressure correction equation is still derived from the conservation of mass. Consequently, the velocity field at each time-level may not satisfy the conservation of mass very accurately and this forms the fundamental difference between the SMAC and PISO. As in the SMAC, the PISO algorithms can not accurately resolve the nonlinear coupling of the u-and v-momentum equations unless the discrete u- and v-momentum equations are solved simultaneously as a single system of equations.

NUMERICAL RESULTS

Numerical results for the polar cavity flow [5] starting from rest

15

and self-sustained unsteady flows over a circular cylinder [2] and a square cylinder [6] obtained using the ITA, SMAC and PISO are presented below. Calculations of the example flows using the ITA and PISO show that the second order implicit time-stepping scheme yields stable numerical results for the time-step size as large as ten times of that for the first order implicit time-stepping scheme. The numerical results presented in this section are obtained using the first order temporal discretization for the SMAC and the second order temporal discretization for the ITA and PISO.

The computational effort for each unsteady flow solution technique depends only slightly on each particular flow problem to be solved, the number of grid points and the number of time-steps, but it depends very strongly on the convergence criteria used. Since the system of equations are solved iteratively using a TDMA [13], one set of convergence criteria needs to be prescribed for the TDMA sweeps. The error norm used for the TDMA sweep is given as;

$$|e|_\ell^1 - |R_{k,\ell}/R_{o,\ell}| < \varepsilon_\ell^1 \tag{29}$$

where $\ell - \{u, v, \text{ or } p\}$ denotes each velocity component and pressure, R_o and R_k are the sums of the absolute residuals of the discrete equation for every grid point evaluated at the initial and at the k-th sweep of TDMA, and ε_ℓ^1 is the convergence criterion for the ℓ-th flow variable. The SMAC and PISO are noniteartive time-advancing schemes, thus only the above set of convergence criteria needs to be prescribed. For the ITA, another set of convergence criteria is needed for the iterative solution of the flow equations. The error norm used for ITA is given as

16

$$|e|_\ell^2 = MAX \ (ABS[(A_{k,\ell}^n - A_{k-1,\ell}^n)/A_{o,\ell}^n]_j \ | j=1,N) < \epsilon_\ell^2 \qquad (30)$$

where $A_{o,\ell}^n$ denotes the maximum ℓ-th flow variable at the n-th

time-level, $A_{k,\ell}^n$ is the ℓ-th flow variable at the k-th iteration, and N

denotes the number of grid points. In the ITA, the flow variables at each

time-level evolve iteratively, thus an accurate solution for each

discrete system of equations at each iteration is not necessary. Hence a

much smaller maximum number of TDMA-sweeps than those for the SMAC and

PISO can be assigned to avoid excessive TDMA-sweeps that can be caused by

eq. (29). The convergence criteria used are $\epsilon_\ell^1 = (1 \times 10^{-7}, 1 \times 10^{-7},$

$1 \times 10^{-2})$ and $\epsilon_\ell^2 = (1 \times 10^{-2}, 1 \times 10^{-2}, 1 \times 10^{-2})$. The numbers of maximum

TDMA-sweeps for the SMAC and PISO are 11, 11, 100 for the discrete u-,

v-, and p-equation, respectively; and those for ITA are 5, 5, 11 for the

u-, v-, and p-equation, respectively. The maximum number of iterations

for the ITA at each time-level is 11. The computational efforts (CRAY/YMP

cpu-time) per each grid point and per each time step for the above

convergence criteria are shown in Table 1. The use of slightly larger

convergence criteria, smaller number of TDMA-sweeps and smaller number of

iterations (for ITA) can decrease the computational effort significantly

without losing the accuracy noticeably.

Polar Cavity Flow Starting From Rest

The lid-driven polar cavity flow is schematically shown in Fig.

1-(a). The Reynolds number based on the lid velocity and the depth of the

cavity is 350. The measured steady state velocity profiles can be found

in Ref. [5]. The flow domain is discretized by 81x81 grid points. The

evolution of u_θ at $(r_y, \theta) = (0.246, 0.0)$ is shown in Fig. 1-(b). The

17

normalized time for the polar cavity flow is based on the lid velocity and the depth of the polar cavity. For a large time-step size ($\Delta\tau=0.05$), the SMAC yields a slightly unstable numerical result at $\tau\approx1$ and the PISO does not yield a convergent solution. The calculated steady state velocity profiles are compared with the measured data in Fig. 1-(c). It is shown in the figure that the velocity profiles obtained using different time-advancing techniques collapse into a single line at each θ-location and that the numerical results are in very good agreement with the measured data.

The mass imbalance for the polar cavity flow, obtained using the large time-step for each time-advancing scheme, is shown in Fig. 2. The mass imbalance produced by the ITA is one order of magnitude smaller than that produced by the SMAC. This result indicate that the ITA can most strongly enforce the conservation of mass and that the use of an under-relaxation do not obscure the numerical results. The ever-increasing mass imbalance produced by the PISO is mostly caused by the second corrector step for which the driving force is the momentum imbalance. For a small time-step size, the three methods yield equally accurate numerical results. However, the trend of the mass imbalance produced by the three methods remains the same as that shown in Fig. 2.

Vortex Shedding Behind a Circular Cylinder

A laminar flow over a circular cylinder at Reynolds number 100 is considered below. The Reynolds number is based on the diameter of the cylinder and the free stream velocity. A survey of measured data and a set of numerical results obtained using the SMAC can be found in Ref. [2]. In Ref. [2], the flow equations transformed onto a cylindrical-polar

18

coordinates were solved using a fully staggered mesh. In the present calculations, the inlet boundary is located at 8r upstream of the circular cylinder, the exit boundary is located at 110r downstream of the circular cylinder, and the side boundaries are located at 8r away from the circular cylinder. The flow domain is discretized by 146x101 grid points in x-, and y-coordinate directions, respectively. A uniform flow is prescribed at the inlet boundary and the vanishing gradient boundary condition is used at the exit boundary. A vanishing normal gradient of the tangential velocity and a vanishing transverse velocity are prescribed at the side boundaries. The flow field is perturbed by twisting the cylinder at the beginning so that the calculated velocity field can initiate the self-sustained oscillatory motion [2].

The streaklines calculated using the PISO are shown in Fig. 3. The streaklines show that the modified PISO can cleanly resolve the vortex shedding behind the circular cylinder.

The calculated Strouhal numbers are compared with the measured data as well as the numerical results by Braza et al. [2] and Eaton [14] in Table 2. The normalized time for flow over a circular cylinder is based on the free stream velocity and the radius of the cylinder. It can be seen in the table that the Strouhal number (for Reynolds number of 110) obtained using a penalty finite element method [14] is smaller than than the measured data. The Strouhal numbers obtained using the three time-advancing schemes, implemented on a pressure-staggered mesh and using the new pressure correction algorithm, are in very good agreement with the measured data.

The velocity vectors and the instantaneous streamlines passing through the separation and/or reattachment locations for the flow over

19

the circular cylinder is shown in Fig. 4. Instantaneous streamlines for unsteady flows are considered to be not meaningful by many researchers as yet. However, a close examination of the streamlines shown in Fig. 4 reveals that the mass flow rate across the streamlines are by far smaller than that along the streamlines. Thus the streamlines passing through the separation and the reattachment locations can be considered as an enclosure of the eddy attached to the cylinder. This interpretation of the instantaneous streamline is similar to that for steady flows. It can be seen in the figure that the attached vortex grows slowly until it becomes almost as large as the circular cylinder, and then the fully grown vortex is swept into the wake region by the nearby free stream. These figures clearly indicate that the low frequency (or the long period) of the vortex shedding is caused by the growth time of the attached vortex. It is also shown in the figure that each vortex shed into the wake region is accompanied by an alternating switching of the reattaching streamline with one of the two instantaneous streamlines passing through the separation locations. Undoubtedly, the instantaneous streamlines help to better understand the vortex shedding mechanism. It is also shown later in this section that the streamlines help to clearly identify the separation and reattachment locations.

The streamline contours and a carpet plot of stream function at t = 0.14T are shown in Figs. 5-(a) and 5-(b), respectively. The saddle point shown in Fig. 5-(b) is caused by a closely spaced counter-ratating vortices, see Ref. [15] for more details.

The evolution of stagnation location in time for flow over a circular cylinder is shown in Fig. 6. It can be seen in Fig. 6-(b) that the numerical result obtained using the PISO exhibits a strong dependence

20

on the time-step size. The amplitude and the phase difference obtained

using the PISO with $\Delta\tau=0.05$ is in worst agreement with the other

numerical results including the one obtained using the same PISO with

$\Delta\tau=0.01$. As the time-step size is decreased, both numerical results

obtained using the SMAC and PISO approach that obtained using ITA. These

results indicate that the ITA yields the most accurate results due to its

capability to resolve the nonlinearity in each component of the momentum

equation and the nonlinear coupling of the u- and v-velocity and the

capability to enforce the conservation of mass most strongly. The strong

dependence of the PISO on the time-step size is caused by the second

corrector step which cause the velocity field less divergence free and by

the linearized momentum equation that yields a solution regardless of the

conservation of mass is rigorously satisfied or not.

The time-varying separation and reattachment locations are shown in

Fig. 7-(a) and 7-(b), respectively. For the flow over the circular

cylinder, the mesh and the time-step size are small enough to accurately

resolve the vortices generated around the smooth cylinder. Thus, the

numerical results obtained using the ITA and SMAC exhibit only a very

small phase difference, while the PISO yields a numerical result that

deviates most from the other numerical results. The reattachment location

presented in Ref. [2] is, in fact, another separation point located at

the symmetric lower part as shown in Fig. 4.

The lift and drag forces are shown in Figs. 8-(a) and 8-(b),

respectively. As in Fig. 7, the numerical results obtained using the ITA

and SMAC are in very good agreement with each other, while the PISO not

only over-predict the amplitude but also yields a significant amount of

phase difference. The present numerical methods yield slightly larger

amplitudes for the lift and drag than those presented in Ref. [2].

Vortex Shedding Behind a Square Cylinder

A laminar flow over a square cylinder at Reynolds number 190 is considered below. The Reynolds number is based on a side of the square cylinder (b) and the free stream velocity. The measured Strouhal number and a numerical result obtained using the ITA can be found in Ref. [6]. In Ref. [6], the flow domain was discretized using a fully staggered mesh and the convection terms were discretized using a formally third order accurate QUICKEST scheme. In the present calculations, the inlet boundary is located at 5.5b upstream of the square cylinder, the exit boundary is located at 35b downstream of the square cylinder, and the side boundaries are located at 5.5b away from the square cylinder. The flow domain is discretized by 131x101 grid points in x-, and y-coordinate directions, respectively. The boundary conditions and the initial perturbations are the same as those used for the flow over a circular cylinder. For the flow over the square cylinder, the numerical methods yield the self-sustained oscillatory motion without the use of the initial perturbation. However, it takes a while for the fully oscillatory motion to be established.

The streaklines calculated using the SMAC are shown in Fig. 9. The streaklines show that the SMAC can cleanly resolve the vortex shedding behind the square cylinder.

The calculated Strouhal numbers are compared with the measured data as well as the numerical results obtained by Davis and Moore using the QUICKEST scheme [6] in Table 3. The normalized time for flow over the square cylinder is based on the free stream velocity and a side of the

square cylinder. It can be seen in the table that the present numerical results are in very good agreement with the measured data, while the numerical results obtained by Davis and Moore deviate further as the mesh is refined. The calculated Strouhal number, which deviates farther from the measured data as the mesh is refined, is caused by the QUICKEST scheme [6].

The velocity vectors and the streamlines for the flow over the square cylinder is shown in Fig. 10. As in the flow over the circular cylinder, the attached vortex grows slowly until it becomes almost as large as the square cylinder, and then the fully grown vortex is swept into the wake region by the nearby free stream. Thus the vortex shedding mechanism and the cause for the low frequency vortex shedding are essentially the same as those for the flow over the circular cylinder. However, in the present case, the attached vortex is split into two parts by the sharp corner and hence, there almost always exists another pair of separation and reattachment locations than the flow over the circular cylinder.

The evolution of stagnation location in time for flow over a square cylinder is shown in Fig. 11. It can be seen in Fig. 11-(b) that the numerical results obtained using different time-advancing schemes yield small phase differences, but all the numerical results exhibit neatly organized oscillatory motion.

The time-varying lift coefficient for flow over the square cylinder is shown in Fig. 12. It can be seen in the figure that the amplitude obtained using the PISO with $\Delta\tau=0.05$ is in worst agreement with the other numerical results including the one obtained using the same PISO with $\Delta\tau=0.01$. As the time-step size is decreased, the amplitudes obtained

using the SMAC and PISO approach that obtained using the ITA. Again, the undesirably strong dependence of the PISO on the time-step size is caused by the second corrector step which cause the velocity field to deviate further from a divergence free velocity field.

The drag for flow over the square cylinder is shown in Fig. 13. For the flow over the square cylinder, the time-step size is not small enough to accurately resolve the initially perturbed flow field. Thus, the numerical results obtained using the different time-advancing schemes exhibit large phase differences. However, all the numerical methods, except the PISO, yield almost the same frequencies and the amplitudes.

CONCLUSIONS AND DISCUSSION

Calculations of a polar cavity flow starting from rest and self-sustained oscillatory flows over a circular and a square cylinders using the ITA (Iterative Time-Advancing Scheme), SMAC (SImplified Marker and Cell) and PISO (Pressure Implicit Splitting of Operators) are presented.

The numerical results show that the SMAC is the most efficient computationally and yields accurate results. Calculations of the lid-driven polar cavity show that the SMAC is even competetive with steady flow solvers to solve steady flows while the ITA, PISO and many other unsteady flow solvers are not [9,15].

The ITA can account for the nonlinearity in each component of the momentum equation and the nonlinear coupling of the u- and v-velocity through the iterative solution of the flow equations. Thus the ITA yields the most accurate numerical results for a large time-step size. The SMAC and PISO are non-iterative time-advancing schemes and hence these methods

24

can only weakly account for the nonlinearity in the Navier-Stokes equations through the use of predictor and corrector steps. As the time-step size is decreased, the numerical results obtained using the SMAC and PISO approach those obtained using the ITA, which shows that the SMAC and PISO can accurately resolve the nonlinearity in the Navier-Stokes equations if a sufficiently small time-step is used.

The SMAC and PISO are quite different in their nature. In the SMAC, the predicted velocity field is corrected to satisfy the conservation of mass and the conservation of momentum is achieved by obtaining a consistent pressure. In the PISO, a second corrector step is introduced to correct the momentum imbalance. The numerical results show that the second corrected velocity field deviates farther from a divergence free velocity field and that the linearized momentum equation yields a solution regardless of the conservation of mass is rigorously satisfied or not. Thus the PISO exhibits an undesirable strong dependence on the time-step size and it is also weakly convergent. These numerical results indicate that accurately enforcing the conservation of mass is very important to enhance the convergence nature as well as to obtain accurate numerical results. The capability of each time-advancing scheme to accurately resolve the unsteady flows is largely attributed to the capability of the new pressure correction algorithm which can strongly enforce the conservation.

Numerical results for flows over a circular and a square cylinders show that a small vortex attached to the cylinder grows very slowly in time until it becomes as large as the cylinder and then the fully grown vortex is shed into the wake region. Each vortex shedding is accompanied by an alternating switching of the reattaching streamline with one of the

25

two streamlines passing through the separation locations, and the alternating switching generates a small attached vortex. Each vortex shedding constitute a half cycle of the self-sustained oscillatory motion. The vortex leaving the cylinder is of the same size as that of the cylinder, and hence the low frequency is caused by the growth time of the attached vortex.

REFERENCES

1. F. H. Harlow and J. E. Welch, "Numerical Calculation of Time-Dependent Viscous Incompressible Flow of Fluid with Free Surface," Physics of Fluids, vol. 8, pp. 2182-2189, 1965.

2. M. Braza, P. Chassing and H. Ha Minh, "Numerical Study and Physical Analysis of the Pressure and Vorticity Fields in the Near Wake of a Circular Cylinder," J. Fluid Mechanics, vol. 165, pp. 79-130, 1986.

3. R. I. Issa, "Solution of the Implicitly Discretized Fluid Flow Equations by Operator-Splitting," J. Computational Physics, vol. 62, pp. 40-65, 1986.

4. R. I. Issa, A. D. Gosman and A. P. Watkins, "The computation of Compressible and Incompressible Recirculating Flows by a Non-Iterative Implicit Scheme," J. Computational Physics, vol. 62, pp. 66-82, 1986.

5. L. Fuchs and N. Tillmark, "Numerical and Experimental Study of Driven Flow in a Polar Cavity," Int. J. Numer. Meth. Fluids, vol. 5, no. 4, pp. 311-329, 1985.

6. R. W. Davis and E. F. Moore, "A Numerical Study of Vortex Shedding from Rectangles," J. Fluid Mechanics, vol. 116, pp. 475-506, 1982.

7. S.-W. Kim, "Numerical Investigation of Separated Transonic Turbulent Flows with a Multiple-Time-Scale Turbulence Model," Numerical Heat Transfer, Part A, vol. 18, pp. 149-171, 1990.

8. S.-W. Kim, "Calculation of Reattaching Shear Layers in Divergent Channel with a Multiple-Time-Scale Turbulence Model," To appear in AIAA Journal, 1991.

9. S.-W. Kim, "Calculations of Separated 3-D Flows with a Pressure-Staggered Navier-Stokes Equations Solver," NASA CR, In

print, 1991.

10. S.-W. Kim and T. J. Benson, "Calculation of a Circular Jet in Crossflow with a Multiple-Time-Scale Turbulence Model," NASA TM, In print, 1991.

11. M Peric, R. Kessler and G. Scheurerer, "Comparison of Finite-Volume Numerical Methods with Staggered and Collocated Grids," Computers and Fluids, vol. 16, no. 4, pp. 389-403, 1988.

12. S. Majumdar, "Role of Underrelaxation in Momentum Interpolation for Calculation of Flow with Nonstaggered Grids," Numerical Heat Transfer, vol. 13, pp. 125-132, 1988.

13. A. D. Gosman and F. J. K. Ideriah, "Teach-T," Dept. of Mech. Engrg., Imperial College, 1982.

14. B. E. Eaton, "Analysis of Vortex Shedding behind a Circular Cylinder by Computer-Aided Flow Visualization," J. Fluid Mechanics, vol. 180, pp. 117-145, 1987.

15. D. S. Jang, R. Jetli and S. Acharya, "Comparison of the PISO, SIMPLER, and SIMPLEC Algorithms for the Treatment of the Pressure-Velocity Coupling in Steady Flow Problems," Numerical Heat Transfer, vol. 10, pp. 209-228, 1986.

TABLE I

Computational Efforts for Each Unsteady Flow Solution Method
(CRAY/YMP cpu-time per each grid point and per each time step)

ITA	SMAC	PISO
1.7×10^{-4}	2.5×10^{-5}	4.5×10^{-5}

(unit in second)

TABLE II

Strouhal Numbers ($S_t = 2fr/U_o$) for Flow over a Circular Cylinder

	ITA	SMAC		PISO		Ref. [2]	Ref. [14]	Exp't
$\Delta \tau$	0.05	0.05	0.01	0.05	0.01	0.01	—	—
S_t	0.158	0.155	0.157	0.164	0.160	0.16	0.147	0.16

TABLE III

Strouhal Numbers ($S_t = fb/U_o$) for Flow over a Square Cylinder

	ITA	SMAC		PISO		Ref. [6]		Exp't
$\Delta \tau$	0.05	0.05	0.01	0.05	0.01	0.05^a	0.05^b	—
S_t	0.133	0.126	0.13	0.142	0.135	0.159	0.165	0.146

(a: 41x40 mesh, b: 51x62 mesh)
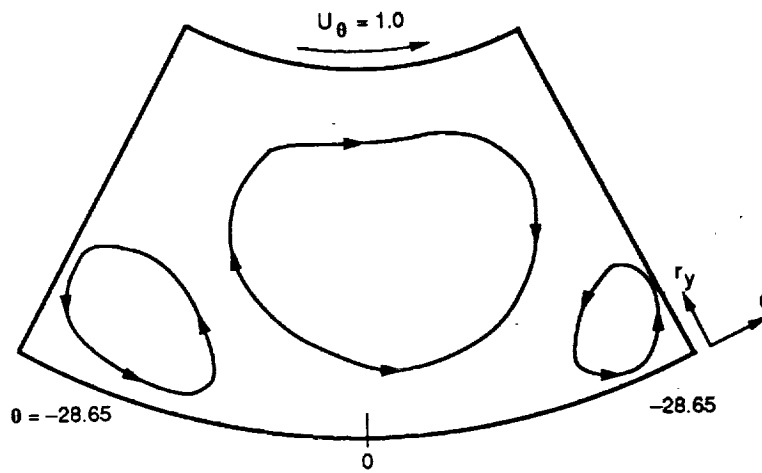
(a) Nomenclature.
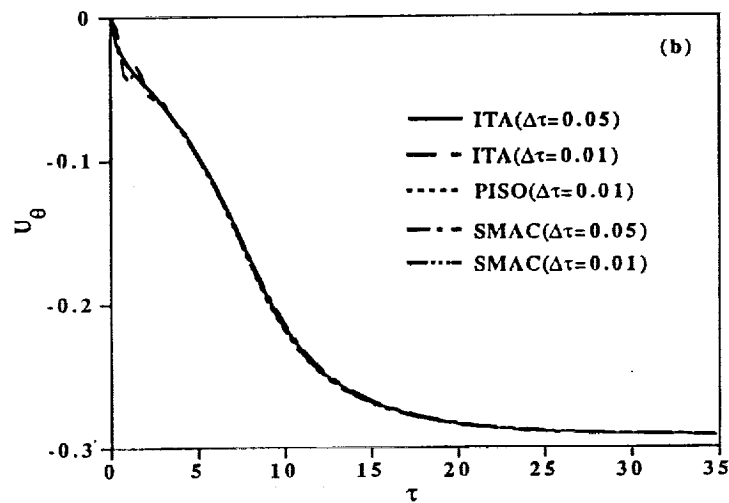
(b) Evolution of u_ϕ at $(r_y, \phi) = (0.246, 0)$.
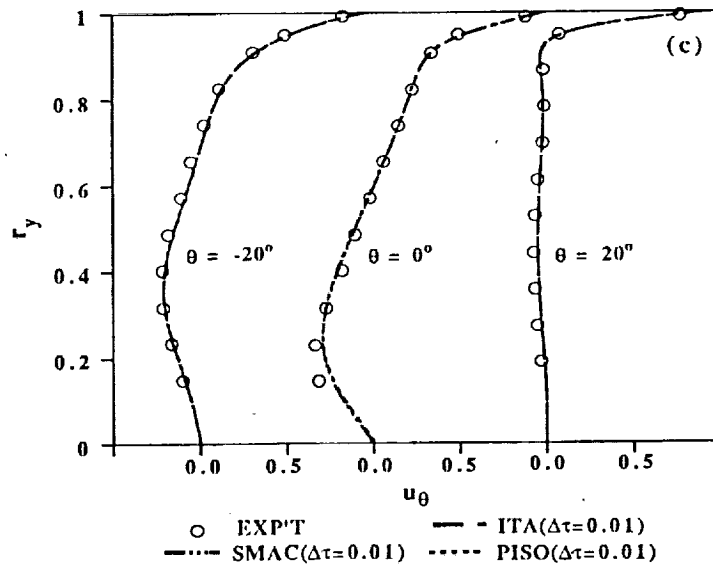
(c) u_θ velocity profiles.

Figure 1.— Polar cavity flow starting from rest.

$$\text{LOG}_{10} |e|_{CM}$$

ITA($\Delta\tau=0.05$) — — — PISO($\Delta\tau=0.05$) — · · SMAC($\Delta\tau=0.05$)
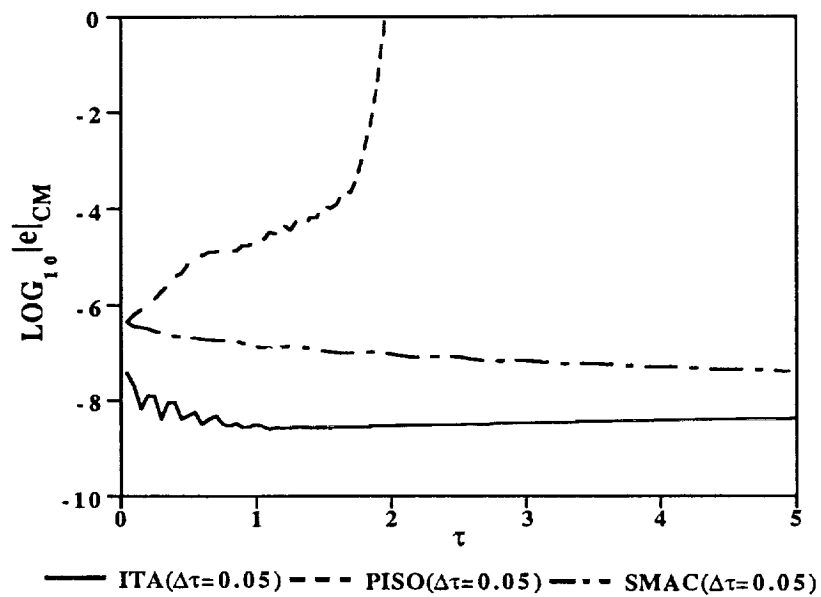
Figure 2.— Mass imbalance.
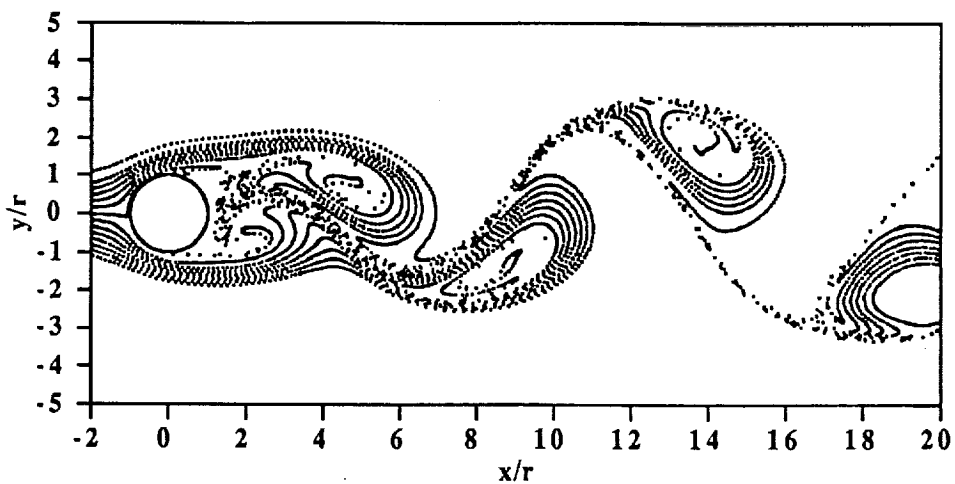
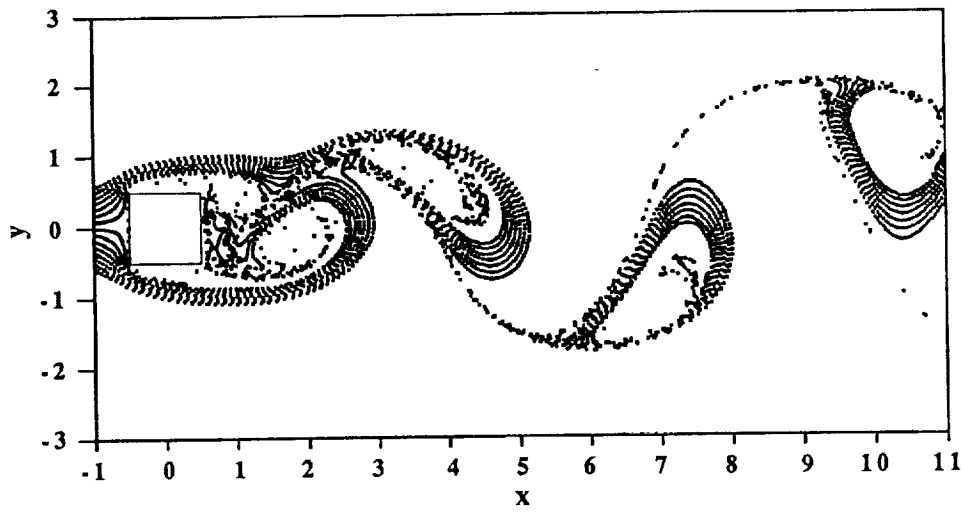

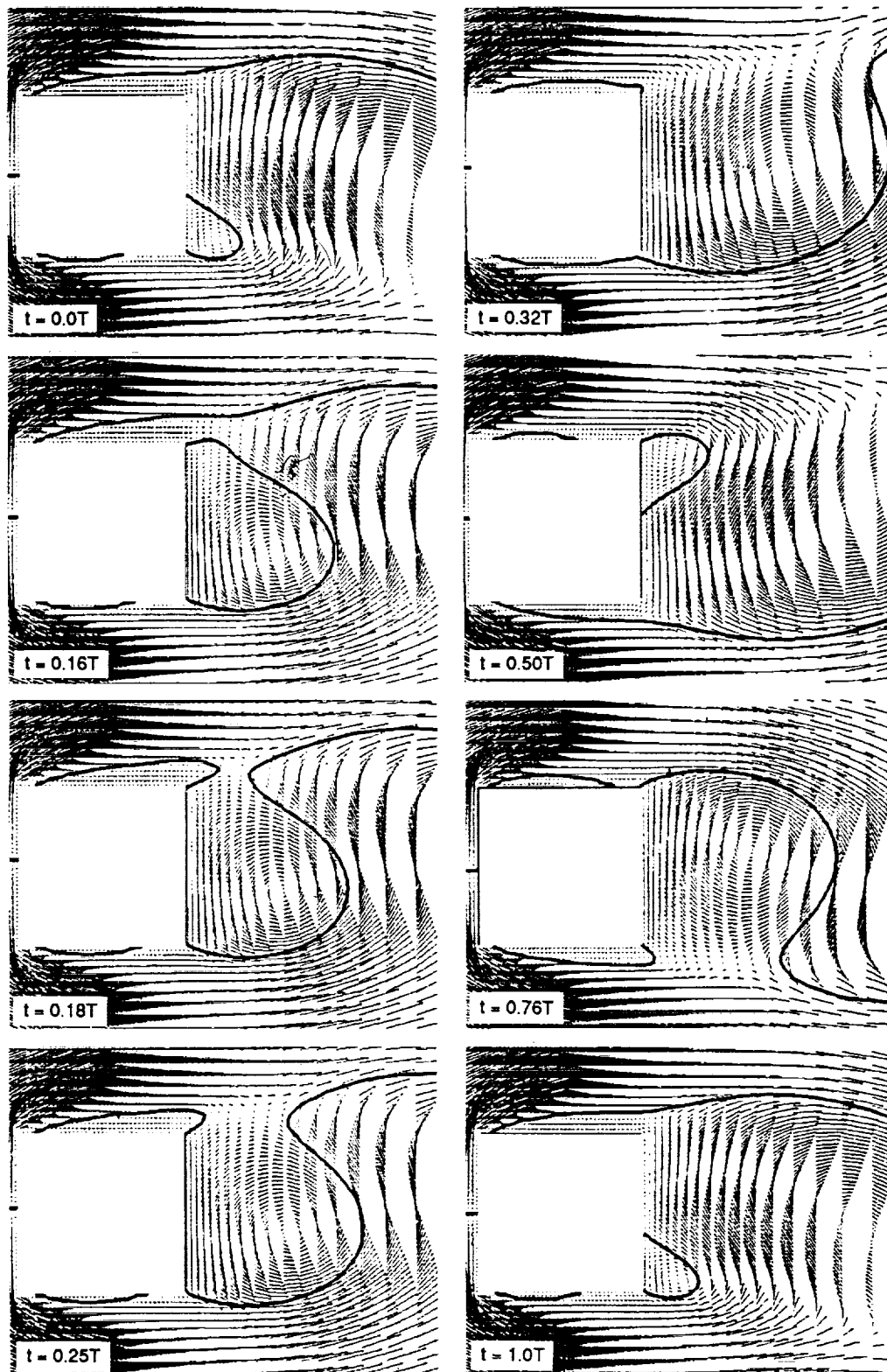Figure 3.— Streaklines for flow over a circular cylinder.
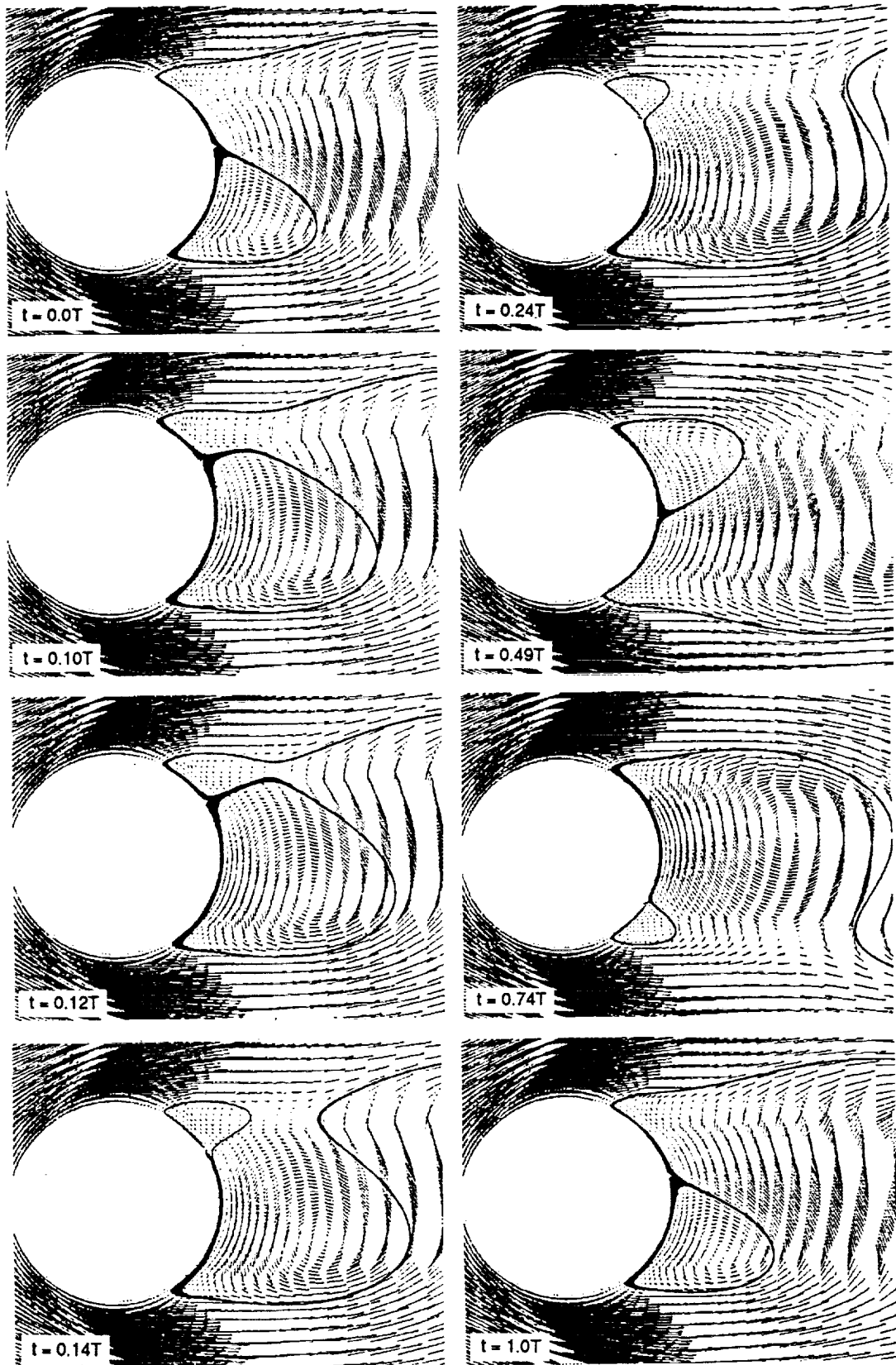
Figure 4.— Velocity vectors and instantaneous streamline contours passing through the separation and reattachment locations.

32
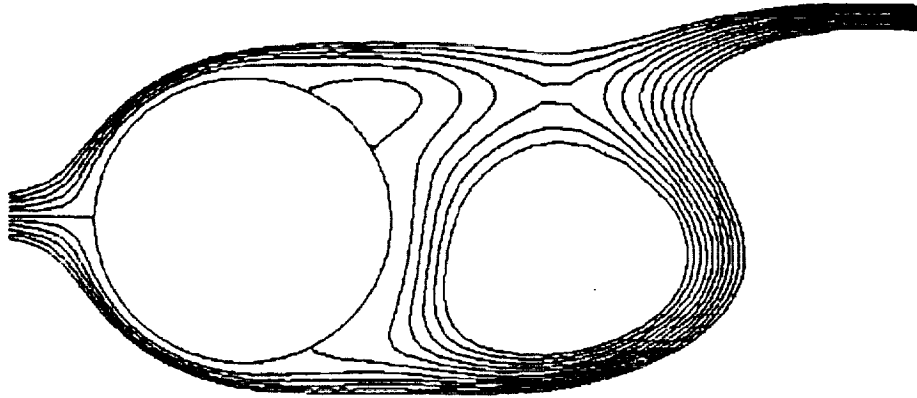
(a) Contour plot.
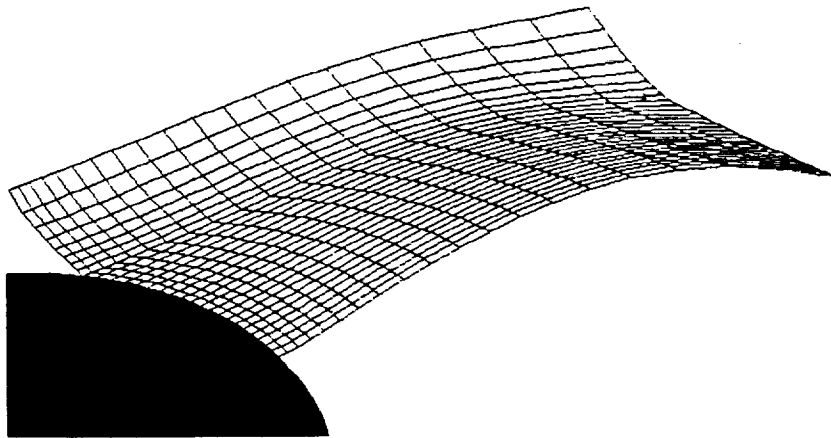
(b) Carpet plot.

Figure 5.— Streamlines at t = 0.14T.

(a) PISO (Δr = 0.01).

ITA(Δτ=0.05) ─ ─ SMAC(Δτ=0.05) ─··─ SMAC(Δτ=0.01)

─ ─ ─ PISO(Δτ=0.05) ····· PISO(Δτ=0.01)
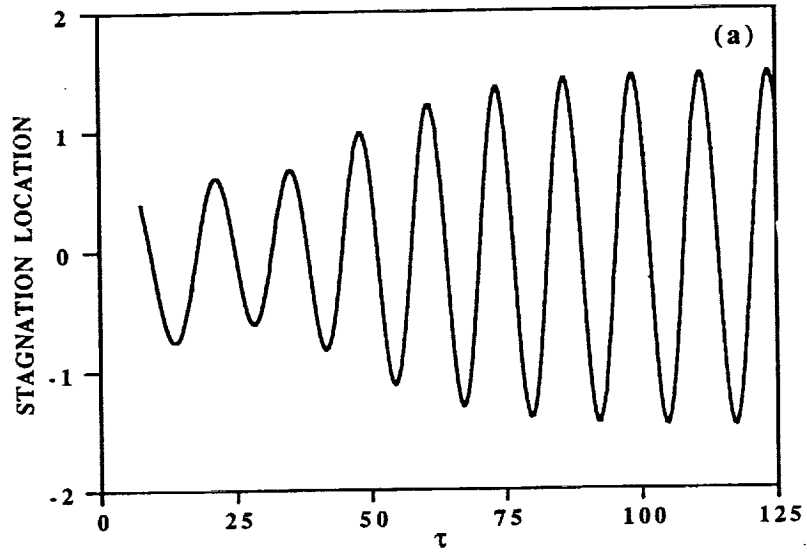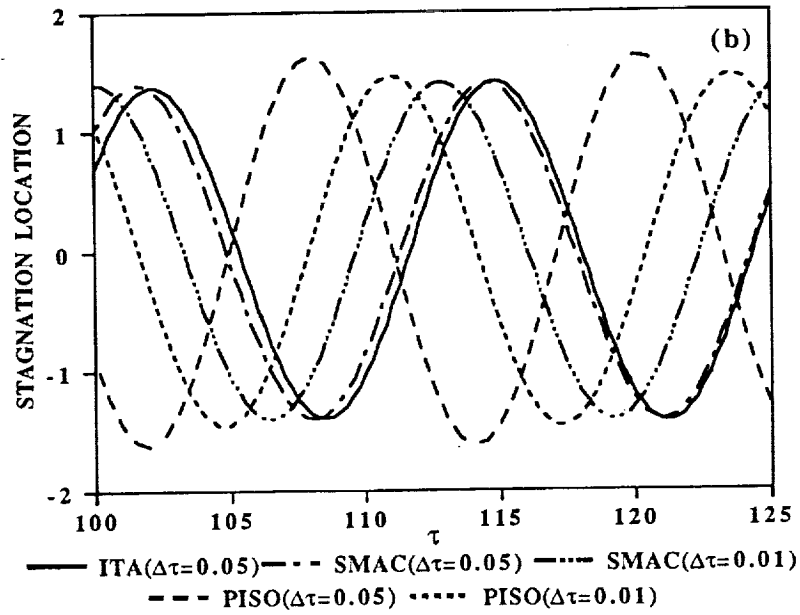
(b) Comparison of ITA, SMAC and PISO.

Figure 6.— Stagnation location for flow over a circular cylinder.

(a) Separation location.

(b) Reattachment location.
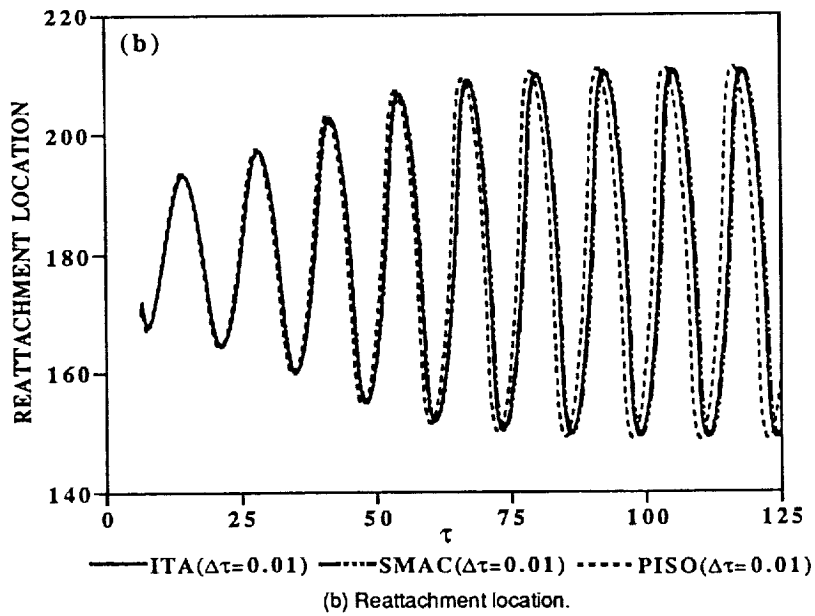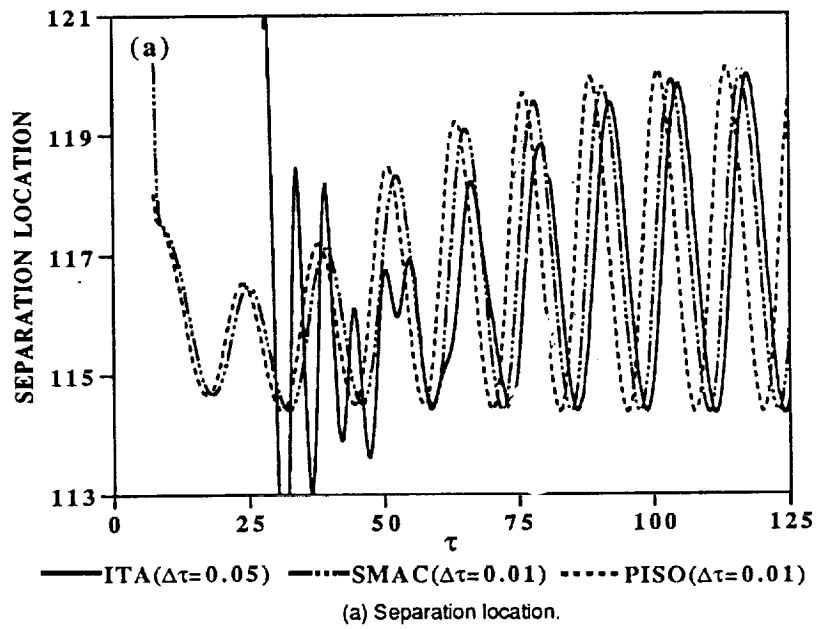
Figure 7.— Separation and reattachment locations for flow over a circular cylinder.

(a) Lift coefficient.

(b) Drag coefficient.
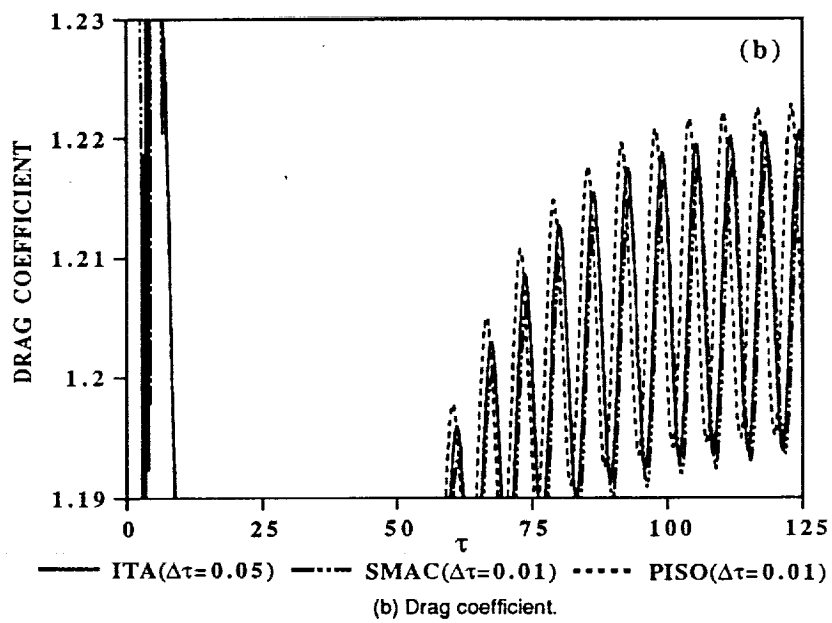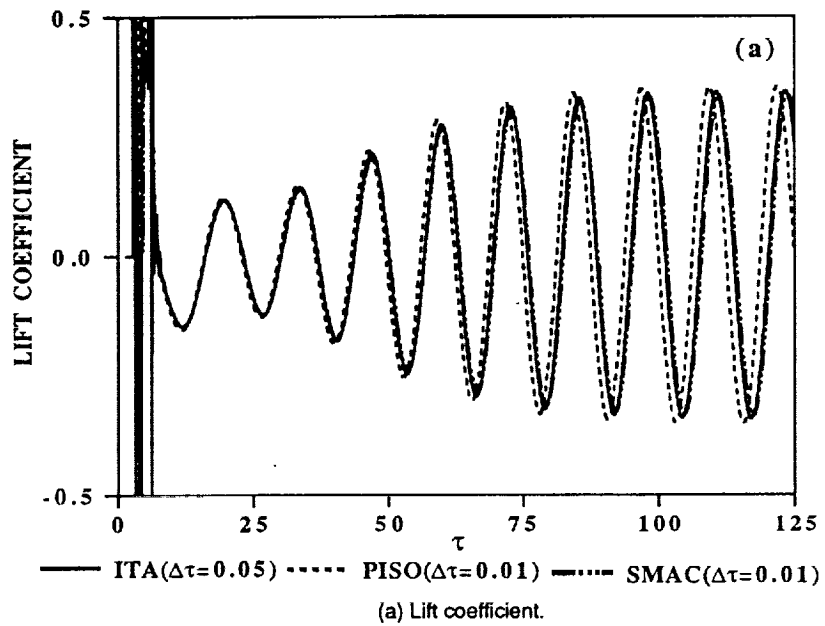
Figure 8.— Lift and drag for flow over a circular cylinder.

Figure 9.— Streaklines for flow over a square cylinder.

Figure 10.— Velocity vectors and instantaneous streamlines passing through the separation a
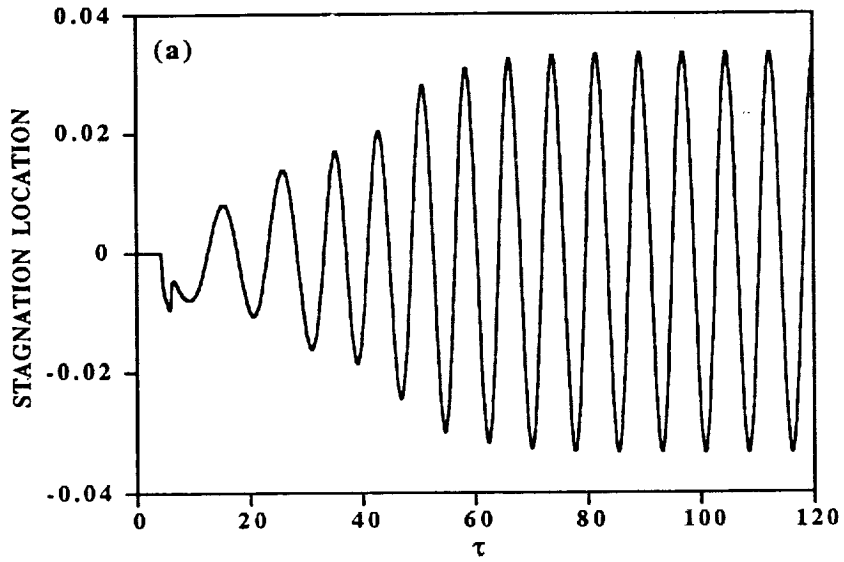reattachment locations.
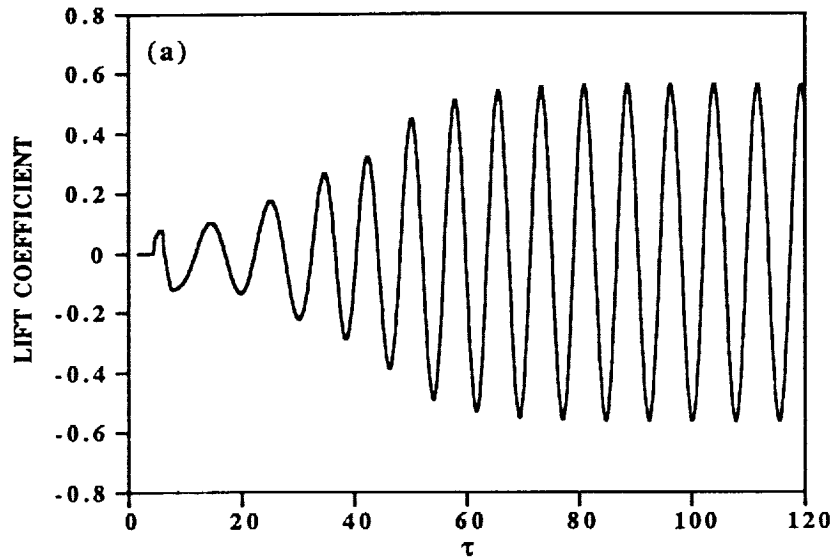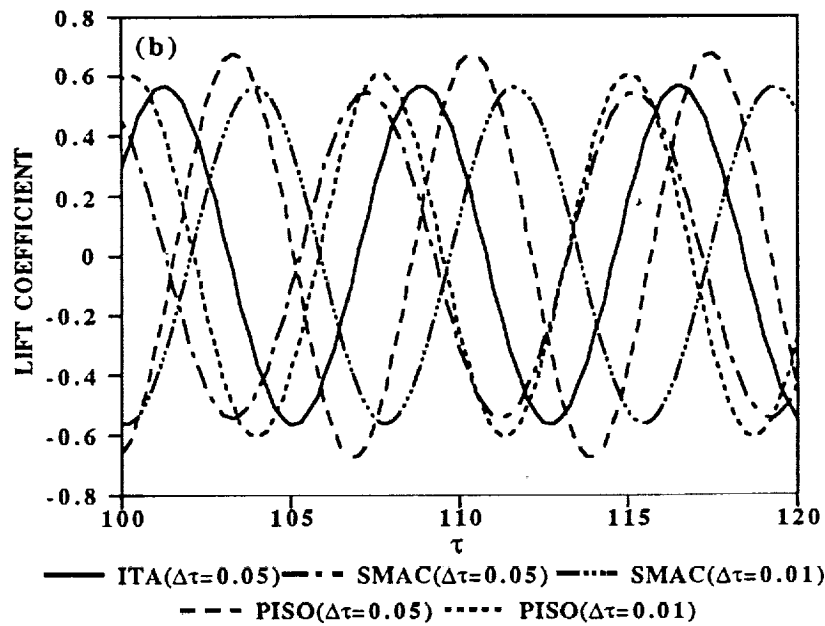
(a) SMAC (Δr = 0.01).

(b) Comparison of ITA, SMAC and PISO.
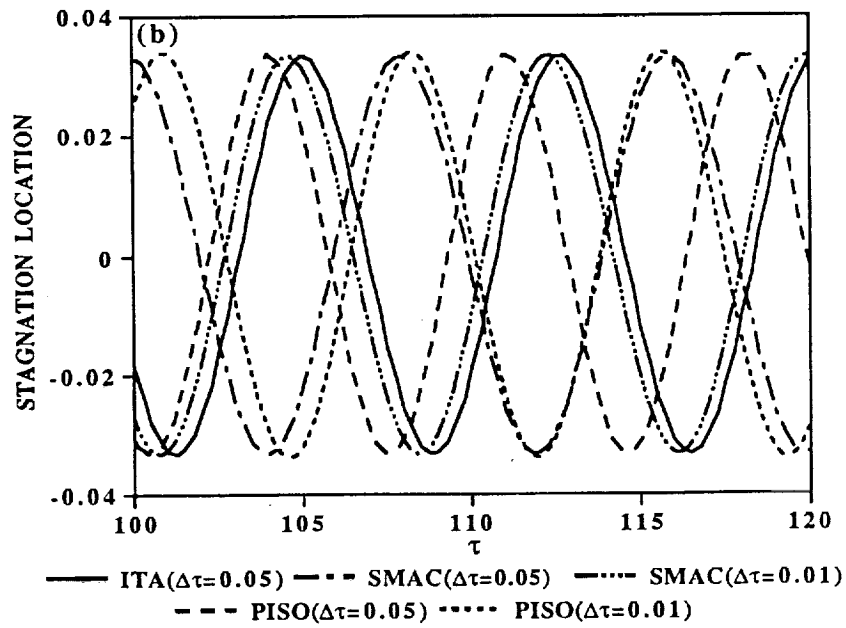
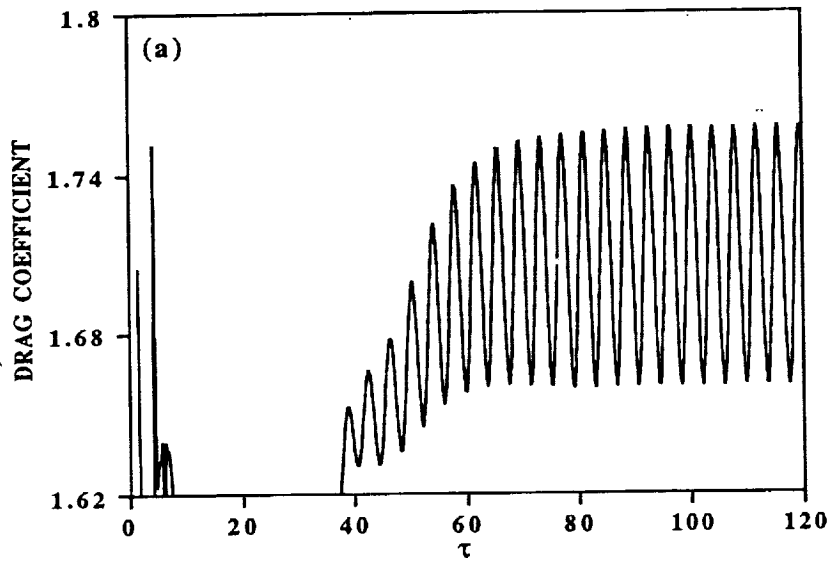Figure 11.— Stagnation location for flow over a square cylinder.
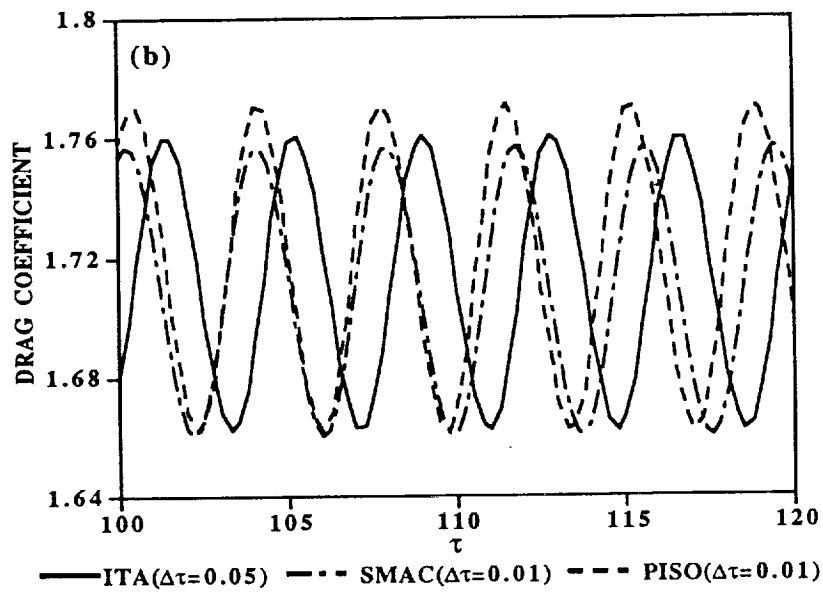
(a) SMAC (Δr = 0.01).

(b) Comparison of ITA, SMAC and PISO.

Figure 12.— Lift for flow over a square cylinder.

(a) SMAC ($\Delta r = 0.01$).

(b) Comparison of ITA, SMAC and PISO.

Figure 13.— Drag for flow over a square cylinder.

NASA
National Aeronautics and
Space Administration

Report Documentation Page

1. Report No. NASA TM – 104406	2. Government Accession No.	3. Recipient's Catalog No.

4. Title and Subtitle	5. Report Date
Comparison of SMAC, PISO, and Iterative Time-Advancing Schemes for Unsteady Flows	June 1991
	6. Performing Organization Code

7. Author(s)	8. Performing Organization Report No.
Sang-Wook Kim and Thomas J. Benson	E – 6232
	10. Work Unit No. 505 – 62 – 52

9. Performing Organization Name and Address	11. Contract or Grant No.
National Aeronautics and Space Administration Lewis Research Center Cleveland, Ohio 44135 – 3191	
	13. Type of Report and Period Covered Technical Memorandum

12. Sponsoring Agency Name and Address	
National Aeronautics and Space Administration Washington, D.C. 20546 – 0001	14. Sponsoring Agency Code

15. Supplementary Notes

16. Abstract

Calculations of unsteady flows using a simplified marker and cell (SMAC), a pressure-implicit splitting of operators (PSIO), and an iterative time-advancing scheme (ITA) are presented. A partial differential equation for incremental pressure is used in each time-advancing scheme. Example flows considered are a polar cavity flow starting from rest and self-sustained oscillatory flows over a circular and a square cylinder. For a large time-step size, the SMAC and ITA are more strongly convergent and yield more accurate results than PSIO. The SMAC is the most efficient computationally. For a small time-step size, the three time-advancing schemes yield equally accurate Strouhal numbers. The capability of each time-advancing scheme to accurately resolve unsteady flows is attributed to the use of a new pressure correction algorithm that can strongly enforce the conservation of mass. The numerical results show that the low frequency of the vortex shedding is caused by the growth time of each vortex shed into the wake region.

17. Key Words (Suggested by Author(s))	18. Distribution Statement
Unsteady flow Vortex shedding Navier-Stokes equation	Unclassified - Unlimited Subject Category 34

19. Security Classif. (of the report)	20. Security Classif. (of this page)	21. No. of pages	22. Price*
Unclassified	Unclassified	42	A03

NASA FORM 1626 OCT 86   *For sale by the National Technical Information Service, Springfield, Virginia 22161